



Ti_{12.5}Zr₂₁V₁₀Cr_{8.5}Mn_xCo_{1.5}Ni_{46.5-x} AB₂-type metal hydride alloys for electrochemical storage application: Part 2. Hydrogen storage and electrochemical properties

K. Young^{a,*}, B. Chao^a, L.A. Bendersky^b, K. Wang^b

^a Ovonic Battery Company, 2983 Waterview Drive, Rochester Hills, MI 48309, USA

^b Material Measurement Laboratory, National Institute of Standards and Technology, Gaithersburg, MD 20899, USA

HIGHLIGHTS

- The gaseous properties of AB₂ alloys were correlated to the phase abundances.
- The electrochemical properties of AB₂ alloys were correlated to the phase abundances.
- AB phase was found to influence storage capacity strongly.
- Zr₇Ni₁₀ phase was found to dominate the kinetic properties.

ARTICLE INFO

Article history:

Received 7 June 2012

Received in revised form

24 July 2012

Accepted 26 July 2012

Available online 3 August 2012

Keywords:

Hydrogen absorbing materials

Transition metal alloys

Metal hydride electrode

Electrochemical reactions

Ni/MH battery

ABSTRACT

In Part 2 of this report, the hydrogen gas charging and electrochemical properties of a series of AB₂-based metal alloys (Ti_{12.5}Zr₂₁V₁₀Cr_{8.5}Mn_xCo_{1.5}Ni_{46.5-x}) designed to have different fractions of Zr–Ni-type secondary phases by varying the Mn/Ni-content were studied to establish correlations of these properties with abundances of the secondary phases. In the gas charging, the general trend of pressure–concentration–temperature slope factor and hysteresis is to diminish with increase in the Zr₇Ni₁₀ phase abundance; the trend of reversible hydrogen storage capacity is to increase as the TiNi-derived AB phase abundance increases. As for the electrochemical properties, the number of activation cycles needed to achieve a given percentage of capacity and power decreases with increase in the total amount of secondary phases. Trends of changes in both the total and reversible capacities follow that in AB phase abundance; the evolution of high-rate dischargeability, bulk diffusion, and surface exchange current is similar to that of Zr₇Ni₁₀ phase abundance – increase in the beginning and decrease afterward as the Mn-content in the alloy increases. Other properties, such as metal–hydrogen bond strength and maximum gaseous phase storage capacity, are predominately dependent on the alloys' composition, i.e. the Mn/Ni ratio.

© 2012 Elsevier B.V. All rights reserved.

1. Introduction

Laves phase-based AB₂ metal hydride (MH)-forming alloys are important candidates to replace the rare earth-based AB₅ MH alloys currently used in nickel/metal hydride (Ni/MH) batteries to address the increasing price of rare earth metals. The flexibility in both stoichiometry [1] and choice of element/structure [2] makes AB₂ alloys more versatile when facing various market requirements. In addition, unlike the AB₅ MH alloys, which require annealing processes to remove unwanted secondary phases, electrochemical properties of the AB₂ MH alloys benefit from a synergetic effect

between the main Laves storage phase and non-Laves secondary phases present in a cast structure and no additional heat treatments are required [3–10]. Therefore, understanding the contributions of the non-Laves phases to storage properties of the AB₂ alloys is essential for improving the performance of the AB₂-based Ni/MH batteries. These non-Laves secondary phases were found to play important roles in the activation, high-rate capability, charge retention, and cycle life of the Ni/MH batteries [11]. In one of the previous reports, the phase abundances in two groups of 16 AB₂ MH alloys designed with various Sn-, Fe-, Al-, and Co-constituencies were correlated with the hydrogen gaseous phase and electrochemical properties [12]. For the first group, the increase in C14 Laves, Zr₉Ni₁₁ and TiNi phases was found to increase the gaseous phase and electrochemical storage capacities and improve the

* Corresponding author. Tel.: +1 248 293 7000; fax: +1 248 299 4520.

E-mail addresses: kyoung@ovonic.com, kwyoung@yahoo.com (K. Young).

charge retention and cycle life, while lowering the hydrogen equilibrium pressure, decreasing the half-cell high-rate dischargeability (HRD), and slightly decreasing the capacity recovery after storage at 45 °C for 60 days. For the second group, containing the C15 Laves phase, ZrNi, and Zr₇Ni₁₀, the effect of the increasing abundance of phase was opposite. In that particular study of the effects of various modifying elements, the changes in secondary phase abundances were not the main design factor but were rather a consequence of varying the level of modifier additions. Although statistically meaningful correlations between properties and phases fractions were found in Ref. [12], the variations in phase abundance with the alloys' compositions were not well designed. Therefore, the current study was designed to follow systematically the changes in secondary phase abundances on the storage properties in a new series of alloys.

In Part 1 of this two-part report, the microstructures of a series of AB₂-based MH alloys (Ti_{12.5}Zr₂₁V₁₀Cr_{8.5}Mn_xCo_{1.5}Ni_{46.5-x}) designed to have different ratios of (Ti,Zr)_xNi_y to (Zr₇Ni₁₀ + Zr₉Ni₁₁) secondary phases by varying the Mn/Ni-content were studied [13]. The trend with increase in the alloys' Mn content was as following: (1) abundance of the major Laves C14 phase increased; (2) abundance of the C15 Laves phase decreased to zero; (3) the secondary phase abundance of the Zr₉Ni₁₁ phase decreased; (4) abundance of the Zr₇Ni₁₀ phase first increased and then decreased; (5) abundance of the TiNi-based AB phase first increased from 0% to 4% and then stabilized at 2%. From the morphology, compositions, and crystallographic orientations of the phases it was concluded that during cooling from the melt the C14 phase was solidified first and formed the core of a dendritic structure, then formation of the C14 phase was followed by a secondary C14' or C15 phase that coated an initial dendrite structure. The inter-dendrite region was occupied by the last-to-solidify melt, which crystallized into the B2 phase and subsequently underwent further solid-state transformation into Zr₇Ni₁₀, Zr₉Ni₁₁, and AB-type phases. In the current report, the gaseous phase hydrogen storage characteristics and electrochemical properties of these alloys are presented and correlated to the phase abundances reported in Part 1.

2. Experimental setup

Details of the sample preparation can be found in Part 1 [13]. Pressure–concentration–temperature (PCT) characteristics for each sample were measured using a Suzuki–Shokan multi-channel PCT system.¹ In the PCT analysis, each sample was first activated by a single, 2 h thermal cycle between 300 °C and room temperature in 2.5 MPa of hydrogen.

Electrochemical properties of the alloys were measured with a powder pressed electrode, without using any binder, in a flooded half-cell configuration. In preparation for the electrochemical studies, each ingot sample was ground and sized using a 200-mesh sieve. The sieved powder was then compacted onto an expanded nickel substrate by a 10-t press to form a test electrode (about 1 cm² in area and 0.2 mm thick) without binder. Electrochemical measurements were performed with a Solartron 1470 cell test multi-channel potentiostat and a Solartron 1250 Frequency Response Analyzer. The discharge capacity of each small-sized electrode was measured in a flooded cell configuration using a partially pre-charged Ni(OH)₂ sintered electrode as the positive electrode and a 6 M KOH solution as the electrolyte. The system was charged at a current density of 50 mA g⁻¹ for 10 h and then discharged at a current density of 50 mA g⁻¹ until a cut-off voltage of

0.9 V vs. the positive electrode was reached. The system was then discharged at a current density of 12 mA g⁻¹ until a cut-off voltage of 0.9 V was reached, and then finally discharged at a current density of 4 mA g⁻¹ until a cut-off voltage of 0.9 V was reached. Linear polarization was performed by scanning the potential from -20 mV to +20 mV of the open circuit voltage at a rate of 0.1 mV s⁻¹. For the potentiostatic discharge experiment, each electrode in a fully charged state was polarized +0.6 V vs. the open circuit voltage for 7200 s.

3. Results and discussion

A series of eight AB₂-based alloys with various Mn/Ni ratios were selected for this study; the designed compositions are listed in Table 1. Mn was chosen as a controlling factor due to its known low solubility in Zr_xNi_y phases (mainly Zr₇Ni₁₀ and Zr₉Ni₁₁), which is expected to affect the presence of these phases [11,14–16]. Inductively coupled plasma analysis showed that the average composition of each arc-melted alloy was very close to the design. Abundances of phases present in the alloys were calculated based on integrated peaks intensities from X-ray diffraction analysis (XRD) and using volume fractions derived from SEM/EDS compositional mapping; the abundances are listed in Table 1.

3.1. Gaseous phase hydrogen storage properties

Gaseous phase hydrogen storage properties of the alloys were studied for PCT characteristics measured at 30, 60, and 90 °C. The resulting absorption (A) and desorption (D) isotherms measured at 30 °C for alloys MN00–MN07 are plotted in Fig. 1a and b. All PCT-related properties of these alloys are summarized in Table 2 and discussed in the following sections.

3.1.1. Mid-point desorption pressure

For the multi-phase AB₂ MH alloys, the PCT isotherms can be considered as the composites of many hydrogen storage sites with various metal–hydrogen bond strengths, which are different from AB₅ MH alloys with simpler phase components [17,18]. Therefore, the PCT isotherms lack a well-defined pressure plateau for the metal (α)–hydride (β) co-existing region. In order to compare the hydrogen equilibrium pressures among the alloys, the mid-point desorption pressure, defined as the pressure where 50% of the desorption is complete, was measured for each alloy and listed in Table 2. The mid-point pressures at different temperatures are used to calculate the entropy and enthalpy of the alloys' reaction (see later sections). In general, as the Mn-content increases, the mid-point desorption pressure decreases. This implies higher metal–hydrogen bond strength in the alloy, which is also consistent with the expanding C14 unit cell volume found in XRD analysis [13]. Compared to Ni, Mn has 3 fewer outer-shell electrons and a smaller electronegativity, which results in a relative reduction of the repulsive force imparted to the electron accompanying an adsorbed hydrogen atom. Similar results were obtained previously for a series of predominantly C14 AB₂ alloys with various Mn/Ni-contents [19].

3.1.2. Slope factor

The slope of the PCT isotherm is related to the disordered nature of the material, which can be attributed to the number of phases present in the alloys [20], substitutional disorder in the multi-component phases [21], composition variations (coring) in the dendrites [19,22,23], and a high density of interphase and inter-domain interfaces [24]. In this study, the slope factor was calculated from the 30 °C desorption isotherms by taking the ratio of the capacities between the middle region (defined as between 0.01 and

¹ The use of brand or trade name does not imply endorsement of the product by NIST.

Table 1

Design compositions and phase abundances estimated from XRD patterns.

Alloy #	Ti (at.%)	Zr (at.%)	V (at.%)	Cr (at.%)	Mn (at.%)	Co (at.%)	Ni (at.%)	C14 phase (%)	C15 phase (%)	Zr ₇ Ni ₁₀ phase (%)	Zr ₉ Ni ₁₁ phase (%)	AB phase (%)
MN00	12.5	21.0	10.0	8.5	2.6	1.5	43.9	34	49	2	15	ND
MN01	12.5	21.0	10.0	8.5	5.6	1.5	40.9	65	23	4	7	1
MN02	12.5	21.0	10.0	8.5	8.6	1.5	37.9	85	8	4	1	2
MN03	12.5	21.0	10.0	8.5	11.6	1.5	34.9	90	4	3	ND	3
MN04	12.5	21.0	10.0	8.5	14.6	1.5	31.9	89	4	2	1	4
MN05	12.5	21.0	10.0	8.5	17.6	1.5	28.9	97	ND	1	ND	2
MN06	12.5	21.0	10.0	8.5	20.6	1.5	25.9	97	ND	1	ND	2
MN07	12.5	21.0	10.0	8.5	23.6	1.5	22.9	98	ND	ND	ND	2

0.5 MPa) and the entire reversible region. The measured slope factor for each alloy is listed in Table 2 and plotted in Fig. 2 as a function of Mn-content. With the increase in Mn-content, the

slope factor remained relatively constant except for a very low value observed on sample NM03.

3.1.3. PCT hysteresis

The PCT isotherm absorption–desorption hysteresis was calculated by the equation,

$$\text{hysteresis} = \ln(P_a/P_d) \quad (1)$$

where P_a and P_d are the absorption and desorption equilibrium pressures at 50% of the reversible storage. The 30 °C PCT hysteresis for each alloy is listed in Table 2 and plotted in Fig. 2 as a function of Mn-content. PCT hysteresis in AB₂ alloys has been demonstrated to be closely related to the unit cell aspect ratio (a/c) of the major C14 phase [25], pulverization rate during gaseous phase cycling [26], and average electron density [27]. It can be speculated that as the a/c aspect ratio increases, the distance for protons to hop along the c -axis decreases. This, in turn, results in a reduction in stress accumulated between the metal and MH phases during the hydriding/dehydriding cycle, and thus less pulverization. In this series of alloys, the hysteresis first decreases, reaches the minimum at alloy MN02, increases, and finally stabilizes as the Mn-content increases.

3.1.4. Hydrogen storage capacity

Both the maximum and reversible storage capacities of alloys MN00 to MN07 are listed in Table 2 and plotted in Fig. 3 as functions of Mn-content. As the Mn-content increases, the maximum storage capacity first increases and then maintains at the maximum level at higher Mn-contents while the reversible storage capacity also increases in the beginning but slightly decreases from the maximum at alloy MN04. The increases in both maximum and reversible storage capacities at lower Mn-contents are due to the increasing hydrogen–metal bond strengths as seen from the decreasing mid-point pressures. The initial increases in capacities also correlate well with the increase in abundance of the C14 phase. With further increase in Mn-content, the maximum hydrogen storage remains about the same due to the limited hydrogen storage in AB₂H₃ stoichiometry (1.57–1.59% by mass fraction depending on the composition). On the other hand, the reversible storage capacity starts to decrease due to the strong metal–hydrogen bonding, which acts as an impediment to hydrogen desorption.

3.1.5. Changes in entropy and enthalpy

The mid-point pressures measured at three different temperatures were used to estimate the heat of hydride reaction (ΔH) and the change in entropy (ΔS). Results for all alloys are listed in Table 2. As the Mn-content increases, both $-\Delta H$ and $-\Delta S$ values initially increase very rapidly and then much more slowly at higher Mn-content. The increase in $-\Delta H$ from 24.6 to 42.3 kJ mol^{−1} agrees with the corresponding expansion of unit cell volume and decreasing mid-point pressure. When the hydrogen storage

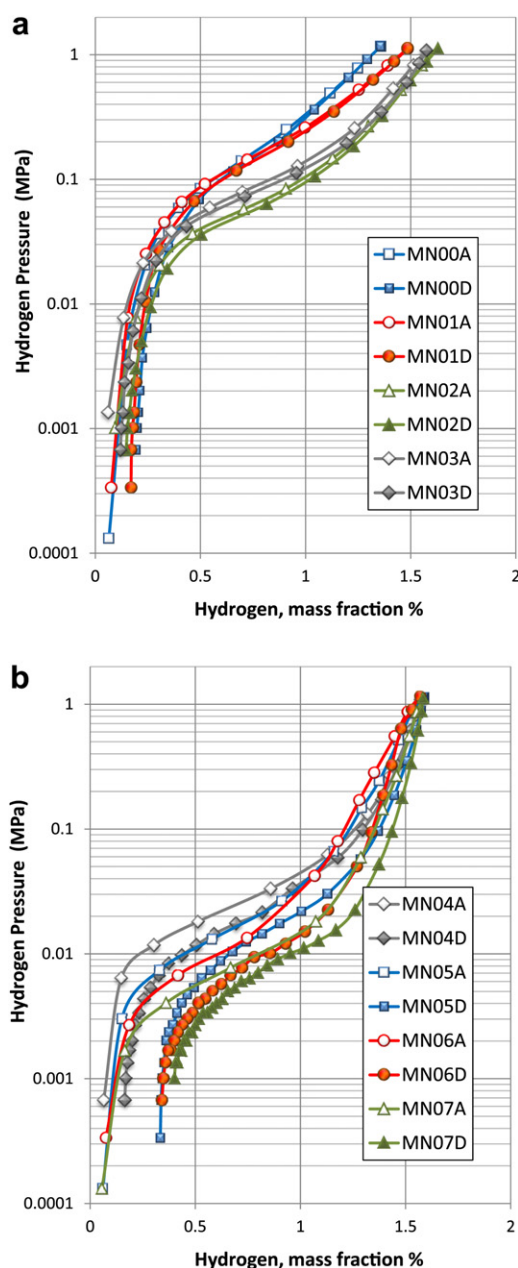


Fig. 1. 30 °C PCT isotherms of MN00, MN01, MN02, and MN03 (a), and MN04, MN05, MN06, and MN07 (b) alloys. Open and solid symbols are for absorption and desorption curves, respectively.

Table 2
Summary of gaseous phase properties and results from half-cell measurements.

Alloy #	Mid-point pressure @ 30 °C (MPa)	Slope factor @ 30 °C (%)	PCT hysteresis @ 30 °C	Max. H-storage @ 30 °C (wt.%)	Rev. H-storage @ 30 °C (wt.%)	$-\Delta H$ (kJ mol ⁻¹)	$-\Delta S$ (J mol ⁻¹ K ⁻¹)	Cycle achieved 90% cap.	Cycle achieved 80% HRD	Cap. @ 50 mA g ⁻¹ (mA h g ⁻¹)	Cap. @ 4 mA g ⁻¹ (mA h g ⁻¹)	HRD	Diffusion coefficient, D (10 ⁻¹⁰ cm ² s ⁻¹)	Exchange current, i_0 (mA g ⁻¹)
MN00	0.090	74.6	1.21	1.00	0.67	24.9	81	1	3	335	361	0.928	2.05	25.05
MN01	0.050	63.8	0.32	1.31	1.05	31.4	98	1	3	344	368	0.935	0.30	64.98
MN02	0.051	67.8	0.12	1.41	1.17	33.8	106	2	6	365	385	0.948	0.57	38.15
MN03	0.014	57.0	0.23	1.58	1.30	38.6	111	3	3	397	416	0.954	0.60	36.79
MN04	0.019	67.2	0.38	1.57	1.41	39.3	116	2	6	367	403	0.911	0.34	32.95
MN05	0.013	69.6	0.46	1.58	1.25	40.0	115	2	4	362	402	0.900	1.96	27.68
MN06	0.009	74.4	0.48	1.57	1.23	40.3	113	4	7	355	402	0.883	1.47	26.34
MN07	0.006	75.4	0.45	1.58	1.18	42.3	117	6	4	313	373	0.839	1.54	17.98

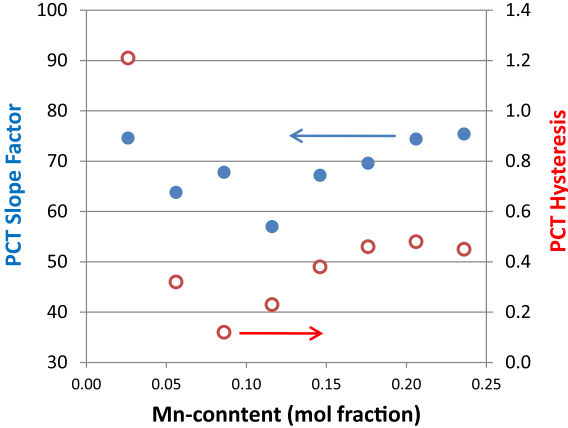


Fig. 2. Plots of PCT slope factor (solid circle) and hysteresis (open circle) as functions of Mn-content.

reaches the maximum for AB₂H₃, further increases in both $-\Delta H$ and $-\Delta S$ are limited. The final ΔS value is the same as the difference in entropies between free hydrogen gas molecules and ordered hydrides [28].

3.2. Electrochemical properties

The electrochemical properties of these alloys were studied only in the half-cell configuration with a flooded electrolyte. The full-cell test results, including cycle life, high-rate, charge retention, and low temperature performance of similar disordered AB₂ alloys with various Mn-contents were reported previously [19].

3.2.1. Capacity measurements

The full capacity, defined as the capacity measured at the slowest discharge rate (4 mA g⁻¹), for the first 13 cycles of each alloy is plotted in Fig. 4a. These electrodes were not activated in hot alkaline solution before the measurements. The cycle number needed to reach 90% of the stabilized capacity indicates the relative level of easiness in the activation process and is listed in Table 2. As the Mn-content increases at the expense of Ni, the alloy becomes more difficult to activate. This finding is in agreement with a previous study on the role of Mn in C14 AB₂ alloys for Ni/MH battery applications [19]. Capacities measured at 50 and 4 mA g⁻¹ rates at the 10th cycle for each alloy are listed in Table 2. As the Mn-content increases, the full capacity (measured at 4 mA g⁻¹)

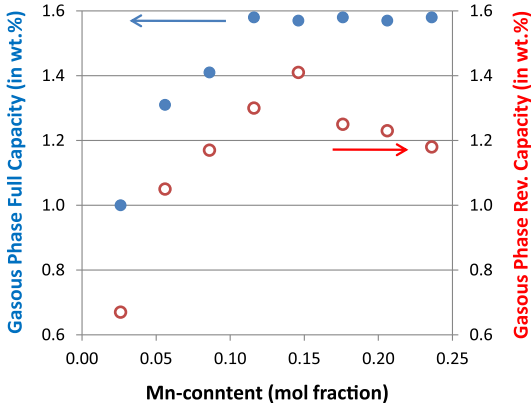


Fig. 3. Plots of gaseous phase maximum capacity (solid circle) and reversible capacity (open circle) as functions of Mn-content.

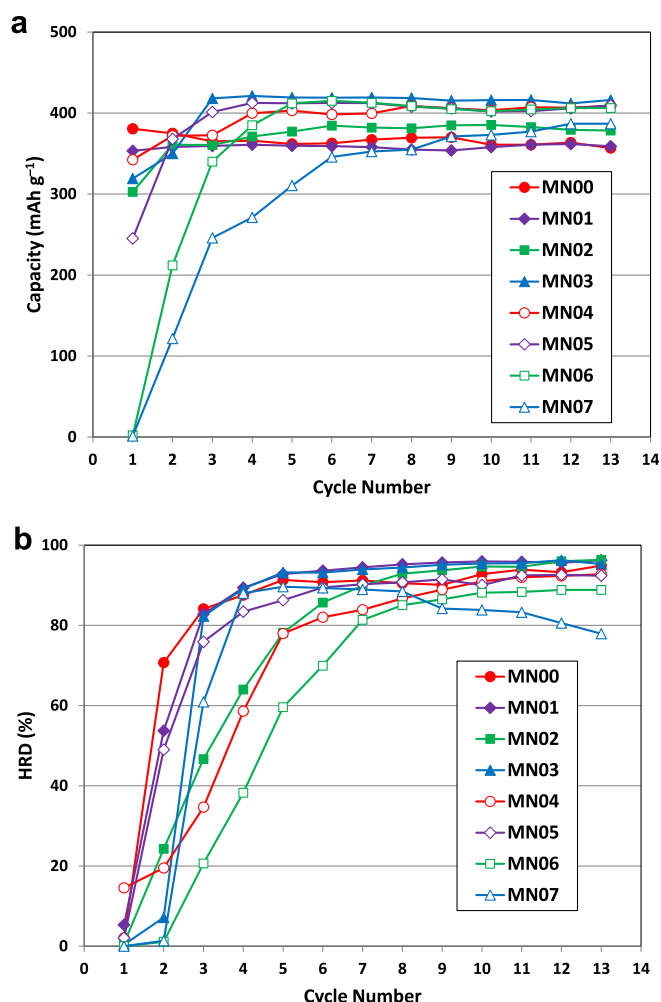


Fig. 4. Plots of capacities measured at a rate of 50 mA g^{-1} (a) and high-rate dischargeabilities (b) of alloys MN00–MN07 for the first 13 cycles.

increases, reaches the maximum at the alloy MN03, maintains at the same level, and finally decreases; the trend is very similar to that of the gaseous phase full capacity. HRD (the ratio between the capacities measured at high rate (50 mA g^{-1}) and low rate

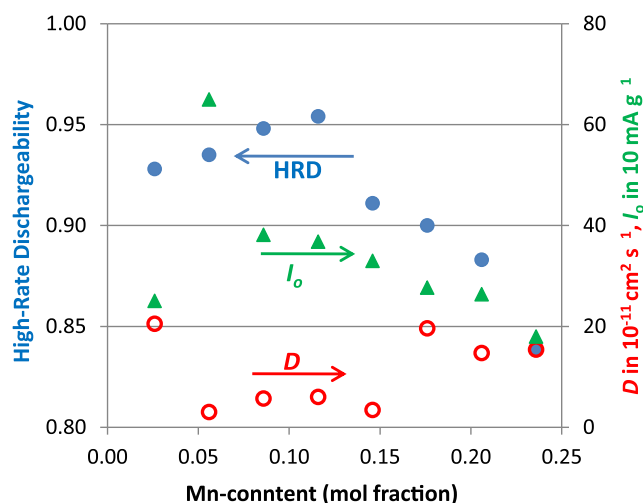


Fig. 5. Plots of high-rate dischargeability, diffusion constant (D), and surface exchange current density (I_0) as functions of Mn-content.

(4 mA g^{-1}) is plotted in Fig. 4b for the first 13 cycles of each alloy in this study. Observed from this figure, the activation in HRD is slower than that in full capacity. The HRD value at the 10th cycle for each alloy is listed in Table 2, which increases and then decreases as the Mn-content increases. The maximum of HRD occurs at alloy MN03. HRD is strongly influenced by the bulk hydrogen diffusion and surface reaction; both are measured and correlated to the HRD values in the next two sections.

3.2.2. Hydrogen diffusion coefficient measurement

The bulk hydrogen diffusions for various alloys were studied electrochemically using a potentiostatic discharge technique [29]. The average diffusion coefficient, D (listed in Table 2 and plotted in Fig. 5 as a function of Mn-content), was calculated from the semi-logarithm of the current response vs. time (Fig. 6) in the later stage of the measurement where the transport property was dominated by diffusion (time $> 2000 \text{ s}$). As the Mn-content in the alloy increases, the D value decreases and then increases, that is opposite to the trend of HRD. Therefore, in the alloys under the current study, the HRD has little connection to the bulk proton transport property.

3.2.3. Exchange current measurement

The exchange current (I_0), a measure of the kinetics in the electrochemical hydrogen reaction at the surface of the electrode, was calculated from the polarization of the electrode using the previously published method [29]. The linear polarization curves of alloys MN00–MN07 with a scan rate of 0.1 mV s^{-1} measured at 50% depth of discharge and room temperature are shown in Fig. 7. I_0 measured for the alloys in this study are listed in Table 2 and plotted in Fig. 5 as a function of Mn-content. The I_0 increases very rapidly in the beginning (peaking at MN01) and then decreases, which is very similar to that of HRD except for alloy MN01. In the current study, the HRD performance of these AB₂ alloys is dominated by the surface reaction.

3.3. Discussion

We attempted to correlate the data presented above on both the gaseous phase hydrogen storage and electrochemical properties of the studied alloys with the microstructures and phase abundances reported in Part 1. In the past, the only study on the individual contributions from Zr₇Ni₁₀ and Zr₉Ni₁₁ was demonstrated in

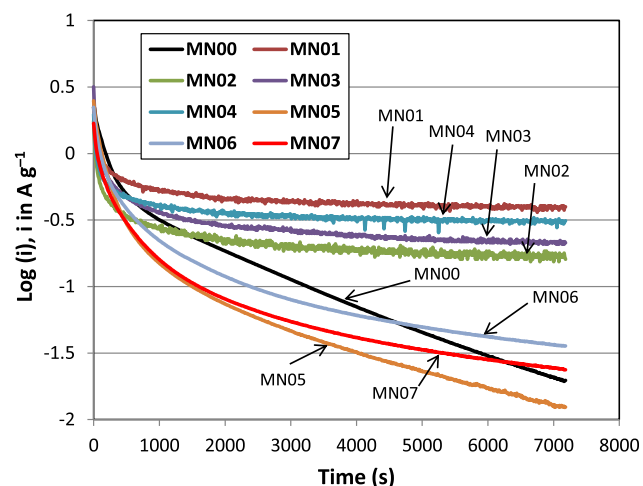


Fig. 6. Semi-logarithmic plots of anodic current vs. time response of alloys MN00–MN07.

Table 3
Correlation factors (R^2) between C15, Zr_7Ni_{10} , Zr_9Ni_{11} , and AB phase abundances and various qualities listed in Table 2. The most significant correlation has been highlighted in **bold**.

Phase	Mid-point pressure @ 30 °C	Slope factor @ 30 °C	Hysteresis @ 30 °C	Max. H-storage @ 30 °C	Rev. H-storage @ 30 °C	$-\Delta H$	$-\Delta S$	Cycle achieved 90% cap.	Cycle achieved 80% HRD	Cap. @ 50 $mA\ g^{-1}$	Cap. @ 4 $mA\ g^{-1}$	HRD	Diffusion coefficient, D	Exchange current, I_0
C14	0.89	0.01	0.53	0.96	0.81	0.93	0.96	0.41	0.24	0.07	0.48	0.18	0.02	0.06
C15	0.88	0.02	0.57	0.97	0.85	0.91	0.97	0.37	0.25	0.10	0.51	0.13	0.04	0.09
Zr_7Ni_{10}	0.25	0.46	0.12	0.12	0.13	0.29	0.16	0.46	0.02	0.21	0.01	0.80	0.50	0.67
Zr_9Ni_{11}	0.82	0.05	0.64	0.95	0.86	0.86	0.93	0.34	0.25	0.14	0.53	0.09	0.07	0.03
AB	0.51	0.17	0.40	0.66	0.86	0.54	0.65	0.08	0.20	0.32	0.63	0.00	0.26	0.01

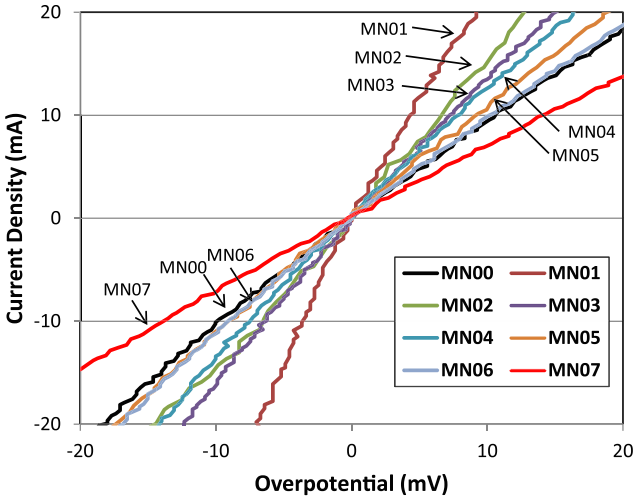


Fig. 7. Linear polarization curves of alloys MN00–MN07 with a scan rate of 0.1 mV s^{-1} measured at 50% DOD and room temperature. The surface exchange current was obtained from the slope measured between -10 and 10 mV overpotential.

a designed orthogonal array (a reduction from 256 to 16 samples without losing the statistical values) with four levels of Sn, Co, Al, and Fe modifiers [12]. In the current study, the difficult part of the analysis is that the linear systematic increase in Mn-content and average electron density results in non-systematic changes in the abundance of the secondary phases. Replacement of Ni (whose radius, r , in a Laves phase alloy is 0.1377 nm [19]) by Mn ($r = 1.428\text{ Å}$) results in an increase in the unit cell volume, increased storage capacity, and decreased plateau pressure [19]. Increasing average electron density has the effect of moving the major phase from C14 to C15. In a previous report the alloys with similar compositions but distinct Laves phases have been studied; the C15 phase was found to have higher gaseous phase hydrogen storage capacity and reversibility, superior HRD, and increased hydrogen bulk diffusion than the C14 phase [11]. Therefore, the systematic changes of properties found in the current study can be attributed directly to the variation in the Mn-content.

In the gaseous phase properties, the general trend of decreasing plateau pressure with higher Mn-content is mainly due to the change in composition of the Laves phases and not related to the abundance of secondary phases. Mn, with a larger atomic radius than Ni, enlarges the lattice unit cell and facilitates the hydride formation. Maximum hydrogen storage capacity and $-\Delta H$ and $-\Delta S$ are also strongly influenced by the Mn content for the same reason. Both PCT slope factor and hysteresis decrease as Zr_7Ni_{10} phase abundance increases in the alloys. In a previous study, the PCT curves of $Zr_xTi_{7-x}Ni_{10}$ ternary alloys exhibited much higher slope factor and hysteresis than those from AB_2 alloys [14]. According to this study slope factor and hysteresis should have positive correlations to the abundance of Zr_7Ni_{10} phase if the effects from the secondary phase are independent from those of the main phase. The found correlations in the opposite direction indicate a more complicated scenario that involves the interaction between the main AB_2 phase and the secondary phases. For example, the inverse trend observed between PCT hysteresis and Zr_7Ni_{10} phase abundance might be due to catalytic contribution from the Zr_7Ni_{10} phase [14]. Higher content of the Zr_7Ni_{10} phase may result in a faster release of hydrogen and reduces the hysteresis. The gaseous phase properties also show the correlation between the reversible hydrogen storage capacity and the AB phase abundance. One possible explanation of this lowering in reversibility is the relative stability of the hydride from the AB phase. For example, a TiNi-type

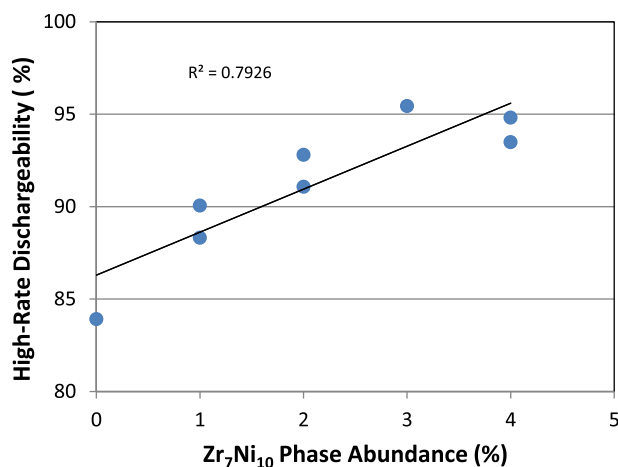


Fig. 8. Plot of high-rate dischargeability as a function of Zr₇Ni₁₀ phase abundance.

B2 phase forms a very stable hydride whose desorption temperature is as high as 550 °C [30], which implies that such a phase should not contribute directly to the reversible storage capacities. Thus, the correlation between the AB phase abundance and the reversible storage capacities might be through the synergetic effect between the phases in contact.

In the electrochemical properties, the number of cycles needed for capacity activation increases as the amount of secondary phases decreases. Usually, phases with higher Ni-contents are easier to activate during the initial cycling [10]. AB (TiNi-type), Zr₇Ni₁₀, and Zr₉Ni₁₁ phases all have a smaller B/A stoichiometric ratio than that of the AB₂ phase. However, due to the low solubilities of V, Cr, and Mn in the phases [16,31,32], the Ni-contents in these non-Laves secondary phases are higher than that in the main AB₂ phase and therefore contribute positively to the activation of the alloy surface. There is no obvious trend found in HRD activation likely due to its complicated nature, which involves creation of new surfaces by both initial pulverization and preferential etching on surfaces, and the presence of catalytic phases on the surface, which may also include oxide, metallic inclusions, pores, and tunnels. The trends in full and high-rate capacities (increasing and then decreasing) are similar to the change in AB phase abundance. The AB (TiNi-type) phase cannot be dehydrided at room temperature in the gaseous phase but can be fully hydrided/dehydrided in the electrochemical environment [33] and therefore contributes to the electrochemical storage capacity. Compared to the AB phase (TiNi-type) with

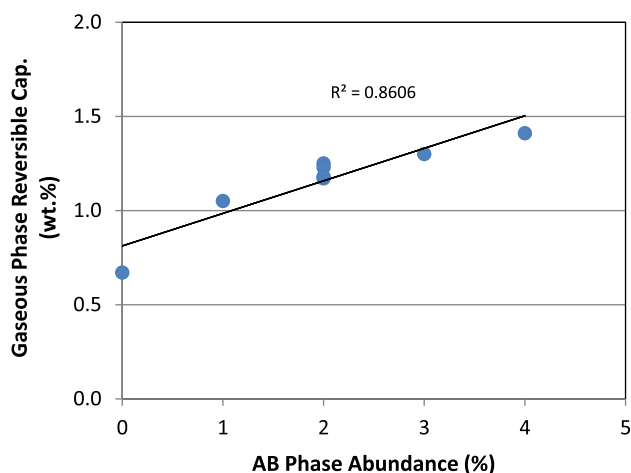


Fig. 9. Plot of gaseous phase reversible capacity as a function of AB phase abundance.

a capacity of 250 mA h g⁻¹ [33], the contributions from the Zr₇Ni₁₀ (110 mA h g⁻¹) and Zr₉Ni₁₁ (90 mA h g⁻¹) [10] phases are smaller. The AB phase can also improve the high-rate dischargeability through the same synergetic effect as in the gaseous phase. HRD and I_0 values, with rapid increases in the beginning followed by decreases as the Mn-content increases in the alloys, follow the same trend in Zr₇Ni₁₀ phase abundance. The positive contribution of Zr₇Ni₁₀ phase to HRD has been reported previously [12].

Correlation factors (R^2) were used to quantify the significance of the identified correlations between the phase abundances and various properties reported in Sections 3.1 and 3.2; the results are listed in Table 3. In the first two rows, the results of the correlations of Laves phases abundances to mid-point pressure, gaseous phase storage capacities, and ΔH and ΔS values are shown. As the C14 phase abundance increases at the expense of C15, the hydride becomes more stable with a stronger metal–hydrogen bond and a higher storage capacity. This finding is different from the conclusion of an earlier study comparing virgin and annealed samples with the same average composition showing C15 phase with a higher hydrogen storage capacity [11]. This variation is because the alloys in this study have different chemical compositions resulting in different metal–hydrogen bond strengths, which supersede the influence from crystal structures. From the XRD analysis, the phase abundance of Zr₉Ni₁₁ was found to have a very similar trend as that of the C15 phase abundance and therefore the similarity of results for C15 (row 2) and Zr₉Ni₁₁ (row 4) is expected (Table 3). The contribution from Zr₉Ni₁₁ cannot be isolated in the current study since the trend of its abundance is masked by similar changes in the main C14 and C15 phases. The Zr₇Ni₁₀ phase abundance has a significant correlation to HRD as was discussed in Section 3.3 (see Fig. 8). Correlations of the AB phase abundance with various properties are shown in the 5th row of Table 3. The AB phase is important to the gaseous phase reversible capacity, and the correlation is plotted in Fig. 9. In the electrochemical properties, AB phase shows more significance in affecting the full capacity rather than the high-rate capacity and therefore has no correlation to HRD. Both ZrNi [4,34] and TiNi [35] are known MH alloys with too strong metal–hydrogen bonds. In the current multi-phase alloys, these AB phases will contribute to the extra electrochemical capacity through the synergetic effect from neighboring phases with higher hydrogen equilibrium pressure [9–12,36].

4. Summary

Both the gaseous phase and electrochemical properties of a series of alloys with systematical changes in the Zr₇Ni₁₀, Zr₉Ni₁₁, and AB (TiNi-type) phase abundances were studied. The contributions from the Zr₉Ni₁₁ phase are difficult to isolate in this series of alloys since the trend of its abundance is masked by similar changes in the main C14 and C15 phases. The Zr₇Ni₁₀ phase is found to affect the electrochemical high-rate dischargeability but not the gaseous phase reversible storage capacity. Further analysis indicates stronger correlation of the Zr₇Ni₁₀ phase with the surface exchange current than with the bulk diffusion coefficient. The AB phase is found to correlate well with the gaseous phase reversible capacity. AB phase is also found to correlate better with the full electrochemical capacity than with the high-rate capacity. The activation becomes more difficult when the total amount of secondary phase abundances decreases.

References

- [1] K. Young, J. Nei, B. Huang, M.A. Fetcenko, Int. J. Hydrogen Energy 36 (2011) 11146.
- [2] S.R. Ovshinsky, M.A. Fetcenko, J. Ross, Science 260 (1993) 176.

- [3] J.M. Joubert, M. Latroche, A. Percheron-Guégan, J. Alloys Compd. 231 (1995) 494.
- [4] J.M. Joubert, M. Latroche, A. Percheron-Guégan, J. Bouet, J. Alloys Compd. 240 (1996) 219.
- [5] J.M. Joubert, D. Sun, M. Latroche, A. Percheron-Guégan, J. Alloys Compd. 253–254 (1997) 564.
- [6] W.K. Zhang, C.A. Ma, X.G. Yang, Y.Q. Lei, Q.D. Wang, Trans. Nonferrous Met Soc. China 19 (1999) 505.
- [7] Q.A. Zhang, Y.Q. Lei, X.G. Yang, K. Ren, Q.D. Wang, J. Alloys Compd. 292 (1999) 236.
- [8] J.C. Sun, S. Li, S.J. Ji, J. Alloys Compd. 404–406 (2005) 687.
- [9] F.C. Ruiz, E.B. Castro, S.G. Real, H.A. Peretti, A. Visintin, W.E. Triaca, Int. J. Hydrogen Energy 33 (2008) 3576.
- [10] F.C. Ruiz, E.B. Castro, H.A. Peretti, A. Visintin, Int. J. Hydrogen Energy 35 (2010) 9879.
- [11] K. Young, T. Ouchi, B. Huang, B. Chao, M.A. Fetcenko, L.A. Bendersky, K. Wang, C. Chiu, J. Alloys Compd. 506 (2010) 841.
- [12] K. Young, J. Nei, T. Ouchi, M.A. Fetcenko, J. Alloys Compd. 509 (2011) 2277.
- [13] L.A. Bendersky, K. Wang, I. Levin, D. Newbury, K. Young, B. Chao, A. Creuziger, J. Power Sources 218 (2012) 474–486.
- [14] K. Young, T. Ouchi, B. Huang, B. Reichman, M.A. Fetcenko, Int. J. Hydrogen Energy 36 (2011) 12296.
- [15] K. Young, T. Ouchi, J. Koch, M.A. Fetcenko, Int. J. Hydrogen Energy 36 (2011) 11137.
- [16] K. Young, T. Ouchi, B. Huang, J. Nei, M.A. Fetcenko, J. Alloys Compd. 501 (2010) 236.
- [17] L. Schlapbach, in: L. Schlapbach (Ed.), Hydrogen in Intermetallic Compounds I: Electronic, Thermodynamic, and Crystallographic Properties, Preparation, Springer-Verlag, Berlin, Germany, 1988, p. 2.
- [18] A.S. Pratt, D.B. Willey, I.R. Harris, Platinum Met. Rev. 43 (1999) 50.
- [19] K. Young, T. Ouchi, J. Koch, M.A. Fetcenko, J. Alloys Compd. 477 (2009) 749.
- [20] S. Lee, J. Yu, H. Lee, K. Jang, J. Lee, J. Alloys Compd. 293–295 (1999) 601.
- [21] Z. Dehouche, M. Savard, F. Laurencelle, J. Goyette, J. Alloys Compd. 400 (2005) 276.
- [22] C.N. Park, S. Luo, T.B. Flanagan, J. Alloys Compd. 384 (2004) 203.
- [23] S. Luo, C.N. Park, T.B. Flanagan, J. Alloys Compd. 384 (2004) 208.
- [24] K. Young, M.A. Fetcenko, F. Li, T. Ouchi, J. Koch, J. Alloys Compd. 468 (2009) 482.
- [25] K. Young, T. Ouchi, M.A. Fetcenko, J. Alloys Compd. 480 (2009) 428.
- [26] K. Young, T. Ouchi, W. Mays, B. Reichman, M.A. Fetcenko, J. Alloys Compd. 480 (2009) 434.
- [27] K. Young, T. Ouchi, M.A. Fetcenko, J. Alloys Compd. 480 (2009) 440.
- [28] L. Schlapbach, A. Züttler, Nature 414 (2001) 353.
- [29] K. Young, T. Ouchi, Y. Liu, B. Reichman, W. Mays, M.A. Fetcenko, J. Alloys Compd. 480 (2009) 521.
- [30] Y. Osumi, Suiso-kyuzo-goukin no Syurui to Sono, New ed., Agune Technology Center, Tokyo, Japan, 1999, p. 261.
- [31] K. Young, T. Ouchi, B. Reichman, W. Mays, R. Regmi, G. Lawes, M.A. Fetcenko, J. Alloys Compd. 489 (2010) 202.
- [32] K. Young, R. Regmi, G. Lawes, T. Ouchi, B. Reichman, M.A. Fetcenko, A. Wu, J. Alloys Compd. 490 (2010) 282.
- [33] S. Wakao, Y. Yonemura, H. Nakano, H. Shimada, J. Less-Common Met. 104 (1984) 365.
- [34] S. Spriano, F. Rosalbino, M. Baricco, P.V. Morra, E. Angelini, C. Antonione, J.-M. Siffre, P. Marcus, Intermetallics 8 (2000) 299.
- [35] C.S. Wang, Y.Q. Lei, Q.D. Wang, J. Power Sources 70 (1998) 222.
- [36] J. Nei, K. Young, R. Regmi, G. Lawes, S.O. Salley, K.Y.S. Ng, Int. J. Hydrogen Energy, submitted for publication.